Technical Sciences, 2022, 25, 87–105

UNIWERSYTET WARMIŃSKO-MAZURSKI W OLSZTYNIE

Yearbook peer-reviewed scientific journal
ISSN 1505-4675
e-ISSN 2083-4527
TECHNICAL SCIENCES
Homepage: https://czasopisma.uwm.edu.pl/index.php/ts/

DOI: https://doi.org/10.31648/ts.7897

EXPERIMENTAL STUDY ON AHMED'S BODY DRAG COEFFICIENT

***Dominik Wysocki*[1], *Arkadiusz Szymanek*[2]**

[1]ORCID: 0000-0002-1990-5382
[2]ORCID: 0000-0002-4235-2368
Department of Thermal Machinery
Faculty of Mechanical Engineering and Computer Science
University of Technology, Częstochowa

Received 15 June 2022, accepted 15 July 2022, available online 15 August 2022.

K e y w o r d s: Ahmed body, aerodynamics, wind tunnel, drag coefficient, boundary layer.

A b s t r a c t

The work presents an experimental designation of the aerodynamic drag coefficient for two configurations of the Ahmed body model, with slant angle of 25° and with the inactive synthetic jet generator. When analyzing the aerodynamic drag of vehicles, most authors focus on higher Reynolds numbers, describing lower values only by designated trend lines. Which is why the main contribution of this experimental work was to designate the Ahmed's body drag coefficient for low Reynolds numbers and to verify the obtained results with other authors experiments especially with the trend lines for Reynolds number in the range 0.35×10^5–1.8×10^5. For data taken from the literature, it can be seen that the value of the drag coefficient for the Ahmed body model decreases when the Reynolds number increases. The results obtained during the experiment show the opposite tendency.

Correspondence: Dominik Wysocki, Katedra Maszyn Cieplnych, Wydział Inżynierii Mechanicznej i Informatyki, Politechnika Częstochowska, al. Armii Krajowej 21, 42-201 Częstochowa, email: dominik.wysocki@pcz.pl.

Introduction

When designing vehicles, it is important to consider fuel consumption and noxious emissions, which are strongly affected by aerodynamics. Therefore, car designers should strive to provide the lowest value of the aerodynamic drag coefficient, so that the medium in which the vehicle moves (air), is as small as possible. Vehicles are slightly affected by aerodynamic forces at low speeds. However, as the speed increases, the air resistance will also increase. Given that the fuel prices are rising, air resistance is now the most important factor in vehicle design. The other forces acting on the vehicle, including the lift force, are negligibly small at the speeds achieved by modern cars (PIECHNA 2000, ZHU et al. 2012).

The dominance of pressure drag and the role of the detachment phenomenon was the reason for the creation of the vehicle model, known today as the "Ahmed body". This model was originally described and characterised in the experimental work of S.R. Ahmed in 1984. The dimensions and shape of the Ahmed body model are shown in Figure 1.

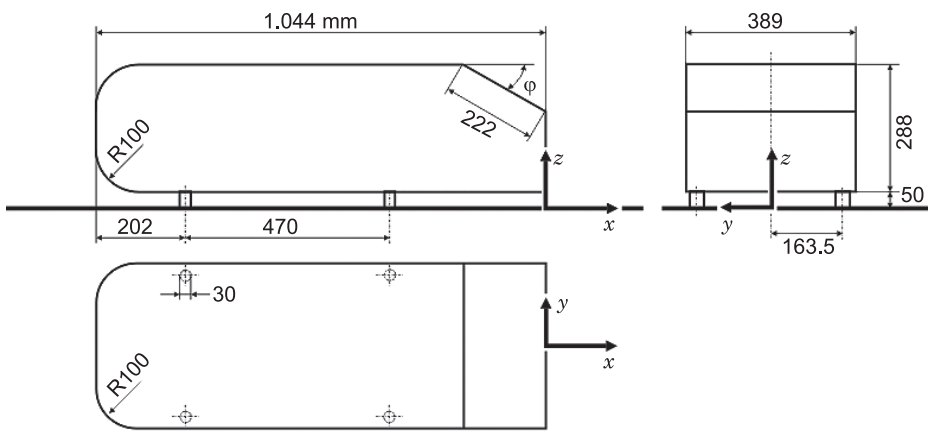

Fig. 1. Dimensions of the Ahmed body model given in millimetres
Source: based on AHMED et al. (1984).

Ahmed body was designed to investigate the effect of angle of inclinationon the drag coefficient of cars. A typical "Ahmed body" consists of three parts. The first, the front of the model has rounded corners on the face to eliminate possible detachment. The second part has a rectangular shape in order to stabilise the flow in front of the inclined angle. The last part is a sloping wall where the boundary layer tear-off zone is located (BELLO-MILLÁN et al. 2016, SHADMANI 2018).

During the experimental research of vehicles aerodynamic drag coefficient, most authors determine its value experimentally only for higher values of the Reynolds number. Smaller values are described with the help of designated trend lines Which is why the main contribution of this experimental work was to designate the Ahmed's body drag coefficient for low Reynolds numbers, corresponding to the speed range of 5-30 km/h and to verify the obtained results with other authors experiments.

Aerodynamic forces

Almost everything that moves through air or water is affected by an aerodynamic force, which is the result of the motion of the object relative to the medium in which it is located. It is caused by the pressure force acting on the body surface and the viscous force resulting from internal fluid friction on the body surface in motion. The components of the aerodynamic force are the aerodynamic drag force (P_x) along the x-axis, which acts along the direction of body motion, and the lift force (P_z) along the z-axis, which acts perpendicular to the direction of motion. There is also a lateral force (P_y) and in addition to these forces, the body may experience and a pitching moment (M_y), a rolling moment (M_x) and a yawing moment (M_z). Traditionally, aerodynamic drag has been determined experimentally by testing the flow of a model or entire vehicle in wind tunnels. The remainder of this paper focuses on the consideration of the aerodynamic drag force P_x analysed in the system of vehicle motion (MAHO 2016, SIVARAJ et al. 2018). An example of the above-mentioned forces and moments are marked in Figure 2.

Aerodynamic drag is a force directed parallel to the direction of motion of a body, which always has the opposite direction of motion of the body. The system of motion is the most effective reference system for testing vehicle aerodynamic drag. Drag depends mainly on: the shape of the object, the square of the velocity of the body relative to the environment in which it is located, the air density and the frontal area of the object. The relationship between the drag and these factors can be expressed as follows:

$$P_x = c_x \cdot \frac{\rho \cdot U^2}{2} \cdot S \quad [\mathrm{N}] \tag{1}$$

where:

c_x – drag coefficient [-],

ρ – gas density $\left[\frac{\mathrm{kg}}{\mathrm{m}^3}\right]$,

U – velocity of the object relative to the medium $\left[\frac{\mathrm{m}}{\mathrm{s}}\right]$,

S – frontal area [m^2].

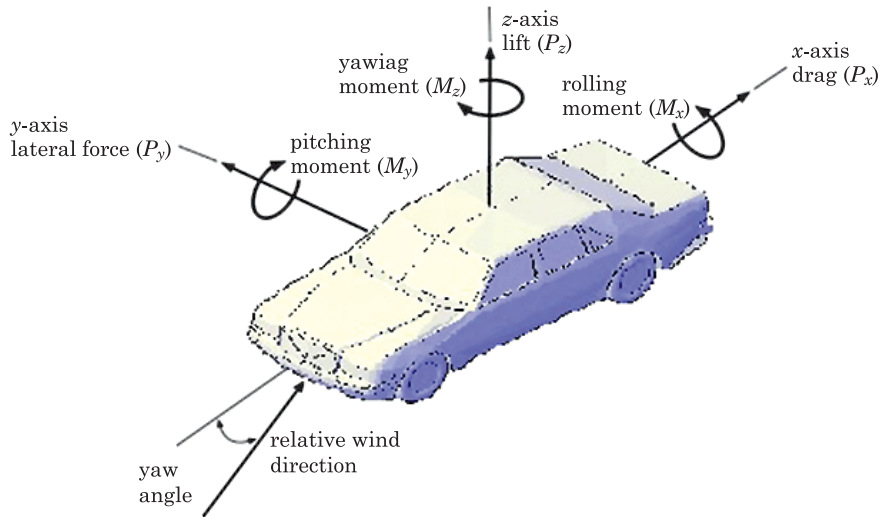

Fig. 2. Moments and forces acting on the car
Source: based on MAHO (2016).

The first part of the equation (1) is the aerodynamic drag coefficient c_x, a measure of the aerodynamic perfection of a body, which determines the dependence of the drag on the shape of the body. It determines how streamlined an object is and depends mainly on its shape. It also depends on the surface area of the body, angle of attack and Reynolds number, however, in the range of speeds reached by mass-produced cars, the above factors have negligible effect.

The drag coefficient determines how streamlined the vehicle is, without providing information on the value of the drag it experiences during motion. The dependence of the resistance on density and the square of velocity determines the dynamic pressure p_d, which is the second part of the equation (1):

$$p_d = \frac{\rho \cdot U^2}{2} \tag{2}$$

The third part of the equation (1) defines the frontal area S, of the test object, which is defined as the largest area of the perpendicular cross-section of the object, relative to the direction of motion. Some companies use a laser beam to accurately measure the actual frontal area of a vehicle. The product of drag coefficient and frontal area c_xS – is called drag factor (MAHO 2016, SIVARAJ et al. 2018).

Aerodynamic drag components

Aerodynamic drag is defined as the force resulting from the pressure distribution around the vehicle (this component is called pressure drag) and from the stresses at the vehicle surface, i.e. friction, which is another component of air resistance called the surface friction drag. Figure 3 illustrates the frictional drag forces F_τ, parallel to the flow direction, and the pressure drag forces F_n, parallel to the flow direction, acting on a small surface element. By summing up the longitudinal components of both components, the total surface resistance of the element is obtained. Adding together the longitudinal force components of all surface elements, results in the total resistance (PIECHNA 2000, TALAY 1975).

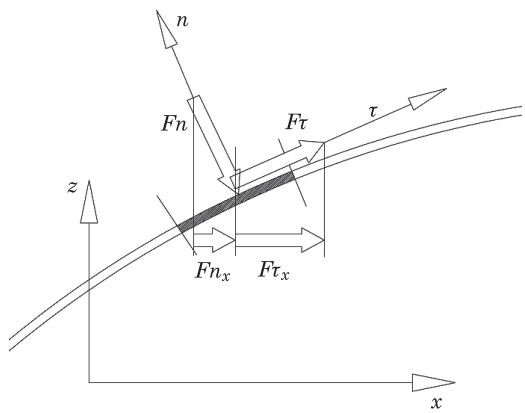

Fig. 3. Components of aerodynamic drag
Source: based on PIECHNA (2000).

Friction drag. The friction drag is closely related to the viscosity of the air, the particles of which adhere to a varying degree to the parts of the vehicle flowing around. As a result of the interaction between the air and the vehicle surface, a region is created in which the fluid velocity changes from zero at the object surface to an undisturbed flow velocity usually denoted U_∞. Air particles directly adhering to the vehicle surface as a result of viscosity, have a velocity of zero. Particles at a certain distance from the vehicle surface have a velocity greater than zero, which increases as the distance from the vehicle surface increases. Air particles at a certain distance from the surface have a maximum velocity equal to the velocity of undisturbed flow. A boundary layer is formed directly on the surface of the streamlined vehicle object, in which the velocity of the particles increases from zero to the velocity of undisturbed flow. The thickness of the boundary layer is smallest at the leading edge and increases as it approaches the trailing edge of the streamlined object. The air particles in

the boundary layer can move in different ways. If the movement of the particles is orderly, along the surface of the streamlined body, this flow is called laminar. If the particles move chaotically, the flow is turbulent (KADIVAR et al. 2021, SCHLICHTING, GERSTEN 2000, TALAY 1975). The velocity distribution in the boundary layer is shown in Figure 4.

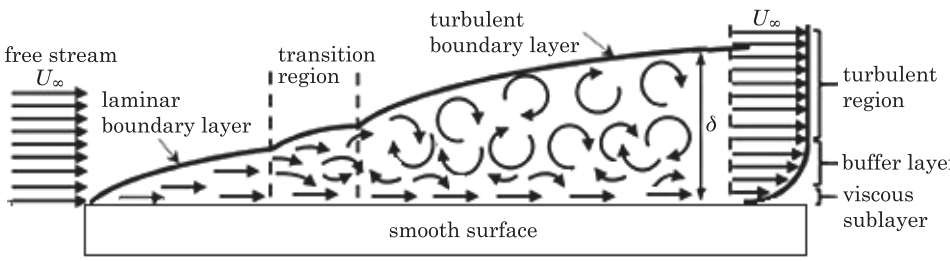

Fig. 4. Velocity distribution in the boundary layer: U_∞ – undisturbed flow velocity, δ – thickness of the boundary layer
Source: based on KADIVAR et al. (2021).

As shown in Figure 4 for a turbulent boundary layer over a smooth surface, a thin layer of laminar flow known as the viscous sublayer forms along the entire length of the surface. The flow in a laminar boundary layer is slowed down by air particles in direct contact with the surface, as the thickness of the boundary layer increases, particles having a higher velocity pull slower particles with them. This process creates turbulence in the turbulent boundary layer, resulting in a surface friction force. This phenomenon is similar to friction of solids and is called viscous friction. In order to reduce the frictional resistance, air particle turbulence must be eliminated by maintaining the laminar character of the boundary layer over as large a surface area as possible (KADIVAR et al. 2021).

Pressure drag. The second component of aerodynamic resistance of road vehicles is pressure drag, also known as shape resistance, which accounts for the greater part of the total air resistance acting on a moving vehicle. The shape resistance of an air moving vehicle depends on the shape of the vehicle, the size of the boundary layer type and the boundary layer detachment phenomenon. Laminar boundary layer gives less frictional resistance, but becomes unstable quickly increasing the shape resistance. The turbulent layer is more stable and adapts better to shape changes, reducing its resistance, but it contributes to an increase in frictional resistance (KADIVAR et al. 2021, SCHLICHTING, GERSTEN 2000, STURM et al. 2012). Detachment of the boundary layer can be analysed from the airflow along a curved surface that may be the surface of the vehicle's roof, specifically the airflow at the end of the roof as shown in Figure 5.

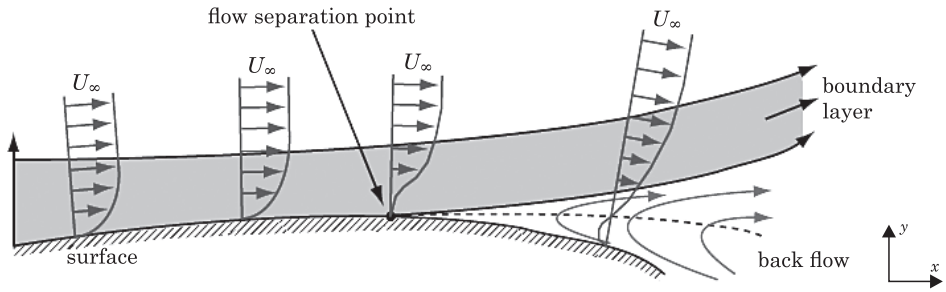

Fig. 5. The phenomenon of detachment of the boundary layer
Source: based on STURM et al. (2012).

The flow velocity of the front part of the car is high, so the pressure in this area is low. As you approach the end of the vehicle roof, the speed of the airflow decreases, and thus the pressure increases. Air particles in the area of the low pressure move to the area of higher pressure, which results in a reduction of their kinetic energy. In the case of a moderate increase in pressure, the air

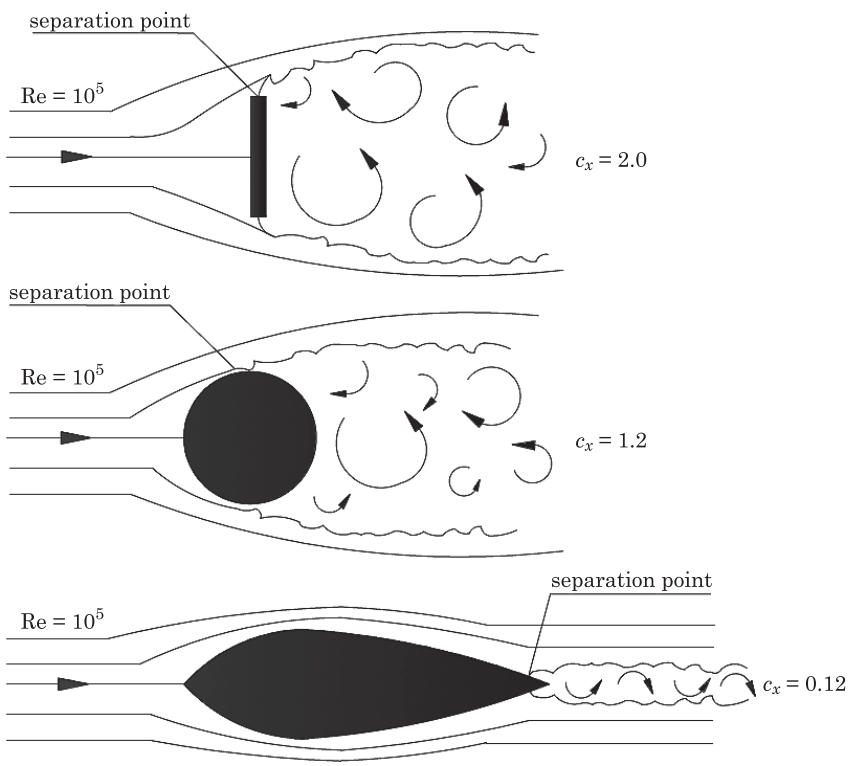

Fig. 6. Air flow around various bodies
Source: based on TALAY (1975).

particles with a higher velocity push the slower particles towards the surface. If the pressure increase is too rapid, the mixing of faster and slower particles is too slow to maintain the movement of the air layers closest to the surface. The boundary layer then ceases to keep up with the change in shape of the streamlined surface and it breaks away. Consequently, we can say that streamlined bodies are bodies in which the boundary layer keeps up with the change of their shape and there is no detachment of the layer. The detachment of the boundary layer can occur in both laminar and turbulent layers, with the difference that the detachment in the turbulent layer occurs later.

When analysing the flow of various bodies: a flat plate, a sphere and an airfoil, it may be noticed that the air flows around each of them as shown in Figure 6. The most disturbed flow occurs in the case of a flat plate, past the point of detachment. The layers of air flowing around the sphere detach after passing the greatest width, and in the case of the airfoil the detachment occurs almost at the end. This results in different sizes of aerodynamic footprints for each body, as the size of the footprint increases, the drag coefficient of the body shape and the total aerodynamic drag cx increase (KADIVAR et al. 2021, MAHO 2016, SCHLICHTING, GERSTEN 2000, STURM et al. 2012, TALAY 1975).

Application of the Ahmed body model

Ahmed body is a good representation of all the most important phenomena that determine the resistance of non-fluid bodies and therefore it is used in vehicle aerodynamics as a reference and a test case. The simple shape of the Ahmed body reduces the number of nodes in the numerical grid and reduces the time required while maintaining the important features of the shape used in modern cars. Testing was carried out using two configurations of a 1:3 scale model of the Ahmed body. The first tested configuration was the basic Ahmed body model with slant angle of 25^{o} the dimensions of which are shown in Figure 7.

For the second arrangement at the sloping wall of the model a metal tube which is an outlet from the concept of synthetic jet generator described in previous work (WYSOCKI 2020) was placed. Next in the pipe with an internal diameter of 3.5 mm and the length of which is equal to the width of the Ahmed body, a 0.1 mm wide slot was milled along the tube from which the air stream outlet was planned. The length of the slot was selected so as to leave 5 mm between the edges of the slot and the Edge of the model on each side. The thickness of the tube was 0.1 mm, after milling the slot, it turned out that the stresses in the tube material deformed the sloth, the width of which was not constant along the tube. This means that the next construction should use a tube with a greater wall thickness. After examining the parameters of synthetic jet generator, it turned out that the synthetic stream generated by the system is too weak to

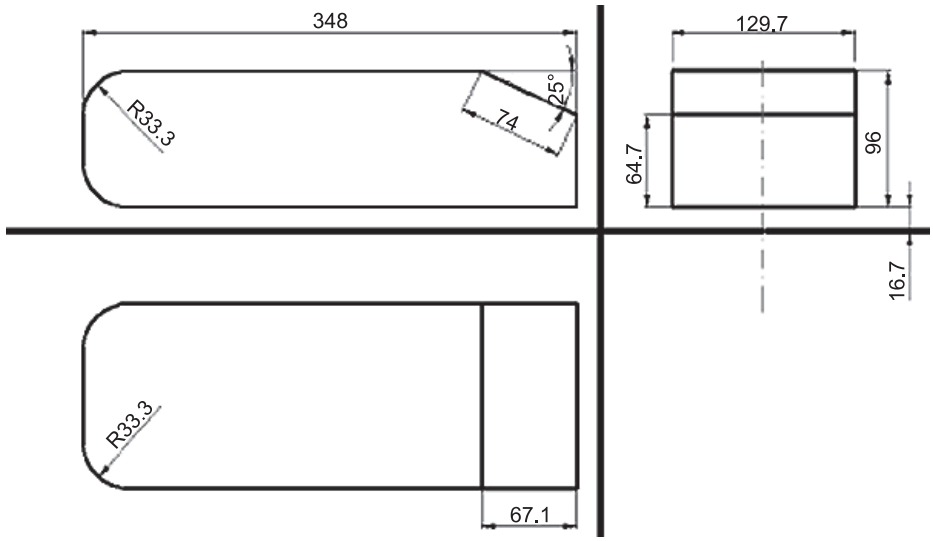

Fig. 7. Ahmed body model in 1:3 scale

control the air flow on the model sloping wall where the boundary layer tear-off zone is located. Ultimately in order to check the aerodynamic drag of the Ahmed body with mounted synthetic stream control system, model shown in Figure 8 was placed in the wind tunnel and the drag coefficient of this configuration was measured and compared with the basic Ahmed body design.

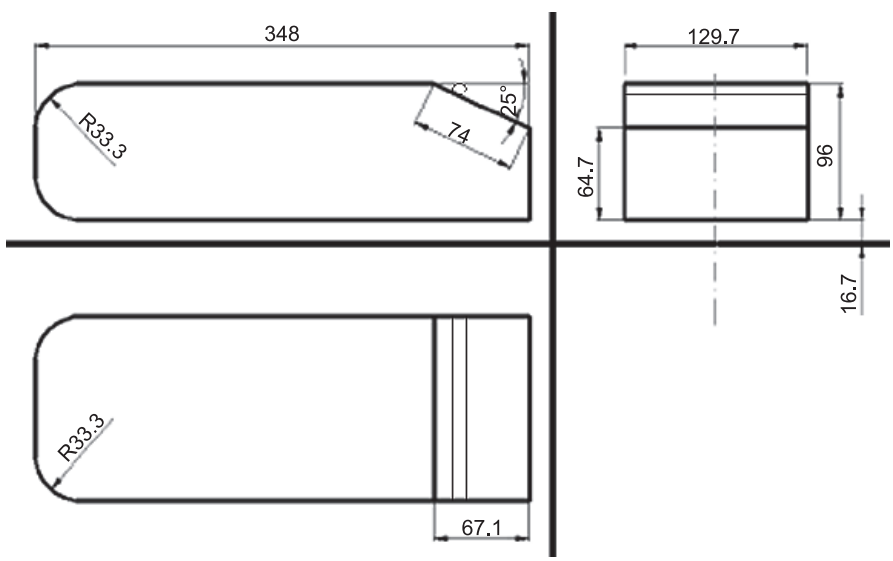

Fig. 8. Conception of Ahmed body model with mounted synthetic jet outlet

Research methodology

Experimental tests were carried in a closed low-speed wind tunnel with a 6 m × 1 m × 1 m test section. The model was placed at the center of the tunnel at a distance of 3 m from the fan. The test stand shown in the Figure 9 includes:

– strut on which the Ahmed body was placed;
– single-component force sensor;
– pulley through which the silk thread was thrown;
– plate on which a variable load was placed during force sensor calibration;
– strain gauge bridge, indications of which were used to determine the force acting on the Ahmed body;
– voltmeter used to record measurement data;
– Prandtl tube for measuring pressure in the tunnel, connected to a Recknagel liquid micromanometer. The probe readings were used to determine the airflow velocity in the tunnel;
– metal support on which the force sensor and micromanometer were placed.

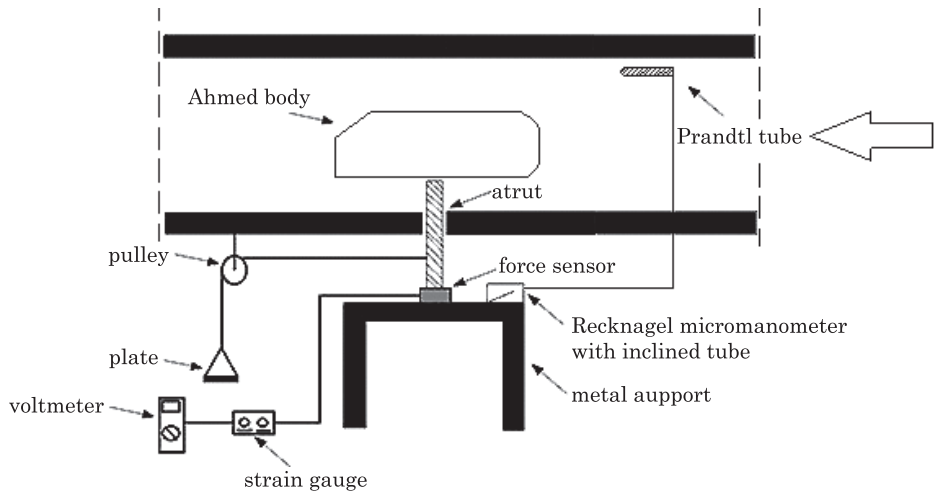

Fig. 9. Diagram of the test stand

Calibration of the single-component force sensor

In order to measure the drag coefficient of the Ahmed body model, a single-component drag force sensor was calibrated by reading the voltage response of the measuring system for successive test loads of the weight, which allows for the performance of the sensor characteristics linking the voltage change on the strain gauge with the force acting on the detector. This plot enables to read out the value of force or mass acting on the detector for a known voltage value.

Calibration was performed without a model placed on the strut and with an Ahmed body model placed on it. Calibration without a model was performed twice to investigate the readings of the balance and the strain gauge bridge while increasing and decreasing the load acting on the instruments, in order to examine the hysteresis of the sensor for both cases and to increase the accuracy of the performed test. However, the calibration with the model was performed only to increase the load acting on the balance.

Before the force sensor was properly calibrated, the force of static friction was checked in the pulley through which the silk thread was thrown, on the ends of which weighing pans of equal weight were hung. One of these was loaded with different weights, the equilibrium of the system was disturbed after using a weight of 0.5 g. During calibration, the voltage change in unloaded balance is measured first. Then the mass of the plate without additional load is taken 11.2 g, from which the mass necessary for imbalance of the pulley was subtracted, equal to 0.5 g. Subsequent measurements began with a 10.7 g load. Then, loads in the form of weights were added, starting with 5 g, and ending with a load of 200 g, in steps of 5 g. The next part of the experiment was to perform a calibration by reducing the load acting on the balance, starting with a load of 200 g and ending with 5 g in steps of 5 g. A further calibration was carried out with the Ahmed body model placed on the strut, only for increasing the load acting on the strain gauge bridge. For each value of load tested, the value of the voltage change on the strain gauge was read from the voltmeter.

Calibration results. The aim of the experiment was to perform the characteristics of the sensor, demonstrating the voltage change at the strain gauge as a function of the force acting on detector. Therefore, the mass loading the plate should be converted into a force according to the equation:

$$F = m \cdot \mathrm{g} \quad [\mathrm{N}] \tag{3}$$

where:

m – mass [kg],
g – gravitational acceleration $\left[\frac{m}{s^2}\right]$.

The final form of the characteristics linking the dependence of the voltage indicated by the voltmeter on the force acting on the sensor without the model and with the Ahmed body model is shown in Figures 10 and 11.

From the obtained characteristics of the method of least squares, trend lines were determined and the equation, by means of which the value of the force acting on the detector can be calculated if the voltage change on the strain gauge bridge is known.

$$y = 0.4468 \cdot x + 0.8799 \tag{4}$$

where:

$y = E$ [V],
$x = P$ [N].

By substituting the quantities under appropriate symbols we obtain:

$$E = 0.4468 \cdot P + 0.8799 \tag{5}$$

Transforming equation (5) we obtain the relation (6), from which we can determine the value of load force acting on the balance for the known value of voltage change on the strain gauge:

$$P = \frac{E - 0.8799}{0.4468} \tag{6}$$

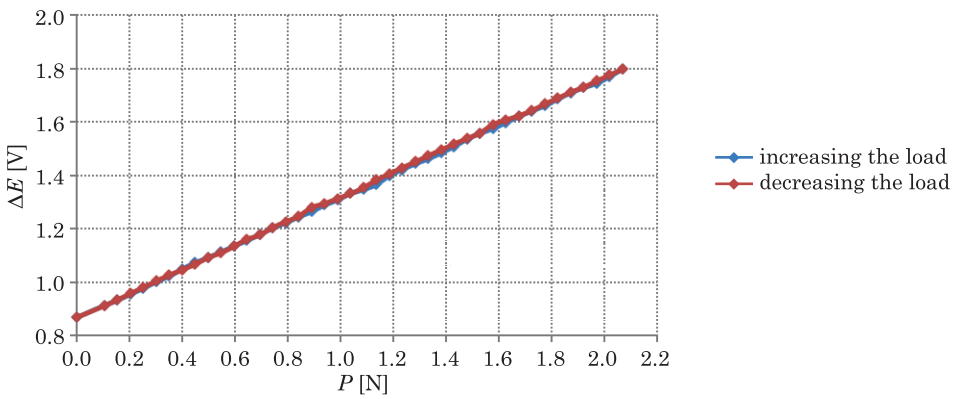

Fig. 10. Dependence of the voltage indicated by the voltmeter on the force applied to the sensor without the Ahmed Body model, for increasing and decreasing the load

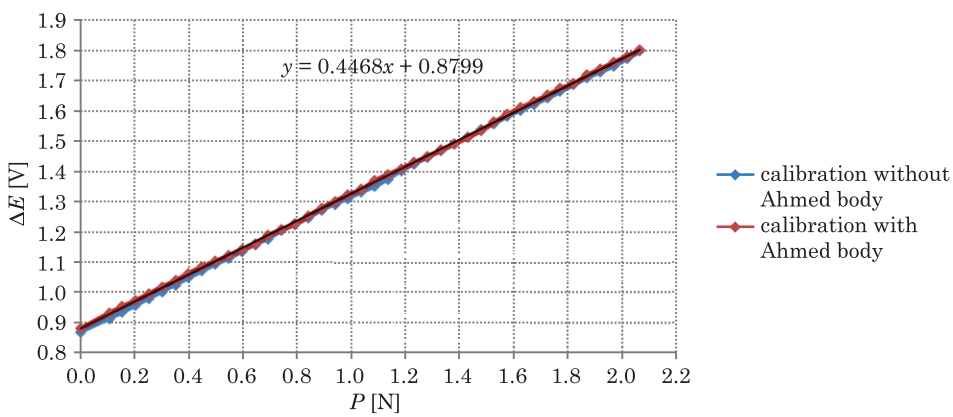

Fig. 11. Comparison of the dependence of the voltage change from the force acting on the sensor for calibration with and without the model

The obtained dependencies of the voltage indicated by the voltmeter on the force acting on the single-component force sensor for measurements without a model and with a model are linear. This means that the detector works properly. Equation (6) will be used in the next part of the experiment, where for the known value of the voltage change on the strain gauge, the value of the drag force loading the model placed on the sensors strut will be calculated.

Determination of the drag coefficient of the Ahmed body model. The experiment began by measuring the environmental parameters – atmospheric pressure and room temperature, followed by the measurement of the manometric liquid temperature, ethanol. Then the ratio of the inclined tube manometer that corresponded to the range of measurements was selected. Next from the read parameters, the following was calculated:

Air density ρ_p:

$$\rho_p = \frac{p}{\mathrm{R} \cdot T} \left[\frac{\mathrm{kg}}{\mathrm{m}^3}\right] \tag{7}$$

where:

ρ_p – air density $\left[\frac{\mathrm{kg}}{\mathrm{m}^3}\right]$,

p – atmospheric pressure [Pa],

R = 287.05 – individual gas constant for air $\left[\frac{\mathrm{J}}{\mathrm{kg} \cdot \mathrm{K}}\right]$,

T – air temperature [K],

Density of the manometric fluid ρ_m. Equation 8 was determined from the plot of manometric fluid (C_2H_5OH alcohol) density as a function of temperature.

$$\rho_m = 825.8 + 0.535 \cdot (293 - T_m) \left[\frac{\mathrm{kg}}{\mathrm{m}^3}\right] \tag{8}$$

where:

ρ_m – density of manometric liquid $\left[\frac{\mathrm{kg}}{\mathrm{m}^3}\right]$,

T_m – temperature of manometric fluid [K].

Dynamic viscosity coefficient of air μ:

$$\mu = \mu_0 \cdot \left(\frac{\left(\frac{T}{T_0}\right)^{1.5} \cdot (T_0 + S)}{T + S} \right) \left[\frac{\mathrm{kg}}{\mathrm{m/s}}\right] \tag{9}$$

where:

μ – dynamic viscosity coefficient of air $\left[\frac{\mathrm{kg}}{\mathrm{m/s}}\right]$,

$\mu_0 = 1.8 \cdot 10^{-5} \left[\frac{\mathrm{kg}}{\mathrm{m/s}}\right]$ – dynamic viscosity coefficient of air in T_0 = 293 [K],

S = 110 K.

T_0 = 293 K.

T – room temperature [K].

Table 1 presents the parameters corresponding to the measurement conditions and the calculated values of air density and manometric fluid density, as well as the coefficient of dynamic air viscosity.

Table 1

Environmental parameters and measurement conditions

T [K]	p_p [Pa]	ρ_p [kg/m^3]	T_m [K]	ρ_m [kg/m^3]	g [m/s^2]	i [-]	μ [kg/ms]
291.65	99,800	1.11921	291.65	826.52	9.81	0.04	0.000018

After defining the measurement conditions, the next step in preparation for the experiment was to place the Ahmed Body model on the strut parallel to the flow direction. The first step in the actual measurement was to switch on the fan. Then, the difference in the level of the manometer liquid was read from the manometer, which allowed us to calculate the flow velocity from the equation (10) and then the Reynolds number from the equation (11).

$$U = \sqrt{\frac{2 \cdot \Delta l_m \cdot \rho_m \cdot \mathrm{g} \cdot i}{\rho_p}} \quad \left[\frac{\mathrm{m}}{\mathrm{s}}\right] \tag{10}$$

where:

U – tunnel air velocity $\left[\frac{\mathrm{m}}{\mathrm{s}}\right]$,

Δ_{lm} – height of manometric liquid column [m],

ρ_p – air density $\left[\frac{\mathrm{kg}}{\mathrm{m}^3}\right]$,

ρ_m – density of manometric liquid $\left[\frac{\mathrm{kg}}{\mathrm{m}^3}\right]$,

g – gravitational acceleration $\left[\frac{m}{\mathrm{s}^2}\right]$,

i – pressure gauge ratio [-].

$$\mathrm{Re} = \frac{\rho_p \cdot U \cdot L}{\mu} \quad [-] \tag{11}$$

where:

Re – Reynolds number [-],

$L = 0.348$ – characteristic dimension (in this case the model length) [m],

ρ_p – density of air $\left[\frac{\mathrm{kg}}{\mathrm{m}^3}\right]$,

U – tunnel air velocity $\left[\frac{\mathrm{m}}{\mathrm{s}}\right]$,

μ – coefficient of dynamic air viscosity $\left[\frac{\mathrm{kg}}{\mathrm{m/s}}\right]$.

The maximum value of the measuring range was selected for the maximum rotational speed of the fan impeller, and the minimum value of the range was selected so that the reading of the height of the manometer liquid column did

not introduce any additional error. The next step of the experiment was to read the voltage values on the strain gauge bridge using a voltmeter. Based on the calibration characteristics of the Ahmed body model, the aerodynamic drag forces for the read voltages were calculated from equation (6).

Knowing the value of the aerodynamic drag force acting on the model, it is possible to calculate the drag coefficient for the tested model and the set air velocity from the equation (12):

$$c_x = \frac{2 \cdot P}{\rho_p \cdot U^2 \cdot S} \; [-] \tag{12}$$

where:

c_x – aerodynamic drag coefficient [-],

P – aerodynamic drag force [N],

ρ_p – air density $\left[\frac{\mathrm{kg}}{\mathrm{m}^3}\right]$,

U – speed of the flowing air $\left[\frac{\mathrm{m}}{\mathrm{s}}\right]$,

$S = 0.01245$ – frontal area of the model [m^2].

In order to check the correctness and reliability of the results, three measurements were made for each configuration of the model. Tables 2-4 presents the results for the basic Ahmed body with slant angle of 25°. Tables 5-7 contain the results for modified model with mounted inactive synthetic jet conception. Figure 12 shows a comparison of the obtained results.

Table 2

Measurement 1 of the basic Ahmed body configuration

Δl_m [m]	U [m/s]	Re [-]	E [V]	P [N]	c_x [-]
0.00510	1.666	38,632	0.8807	0.0018	0.087
0.02200	3.460	80,237	0.8892	0.0208	0.234
0.03450	4.333	100,478	0.9035	0.0528	0.379
0.06900	6.127	142,098	0.9332	0.1193	0.428
0.11400	7.876	182,648	0.9734	0.2093	0.455

Table 3

Measurement 2 of the basic Ahmed body configuration

Δl_m [m]	U [m/s]	Re [-]	E [V]	P [N]	c_x [-]
0.00493	1.638	37,983	0.8810	0.0025	0.124
0.02221	3.476	80,619	0.8913	0.0255	0.284
0.03423	4.316	100,085	0.9040	0.0539	0.390
0.06927	6.139	142,376	0.9281	0.1079	0.386
0.11416	7.881	182,777	0.9696	0.2008	0.435

Table 4

Measurement 3 of the basic Ahmed body configuration

Δl_m [m]	U [m/s]	Re [-]	E [V]	P [N]	c_x [-]
0.00489	1.631	37,828	0.8802	0.0007	0.034
0.02186	3.449	79,981	0.8897	0.0219	0.248
0.03404	4.304	99,806	0.9031	0.0519	0.378
0.06886	6.121	141,954	0.9316	0.1157	0.416
0.11439	7.889	182,962	0.9712	0.2043	0.442

Table 5

Measurement 1 of the Ahmed body with mounted outlet of inactive synthetic jet

Δl_m [m]	U [m/s]	Re [-]	E [V]	P [N]	c_x [-]
0.00500	1.649	38,251	0.8821	0.0049	0.244
0.02000	3.299	76,503	0.899	0.0427	0.529
0.03411	4.308	99,909	0.916	0.0808	0.587
0.06850	6.105	141,582	0.949	0.1547	0.559
0.11405	7.878	182,688	0.980	0.2240	0.486

Table 6

Measurement 2 of the Ahmed body with mounted outlet of inactive synthetic jet

Δl_m [m]	U [m/s]	Re [-]	E [V]	P [N]	c_x [-]
0.00487	1.628	37,751	0.8826	0.0060	0.307
0.02023	3.318	76,942	0.898	0.0405	0.496
0.03320	4.250	98,567	0.916	0.0808	0.603
0.06813	6.089	141,199	0.951	0.1591	0.578
0.11421	7.883	182,817	0.981	0.2263	0.491

Table 7

Measurement 3 of the Ahmed body with mounted outlet of inactive synthetic jet

Δl_m [m]	U [m/s]	Re [-]	E [V]	P [N]	c_x [-]
0.00491	1.635	37,906	0.8816	0.0038	0.192
0.01987	3.288	76,254	0.900	0.0450	0.561
0.03498	4.363	101,175	0.915	0.0786	0.556
0.06873	6.115	141,820	0.950	0.1569	0.565
0.11389	7.872	182,560	0.979	0.2218	0.482

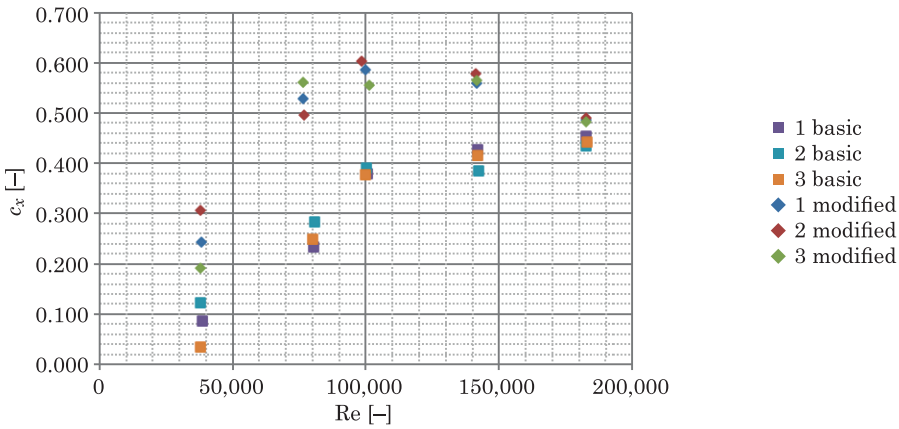

Fig. 12. Comparison of the obtained results

The obtained dependences of the voltage indicated by the voltmeter on the force acting on the force sensor are linear, which means that the detector works properly. The velocities obtained during the tests indicate that the fan generating the flow is stable enough that the measurements carried out in the used tunnel achieve good accuracy The results obtained for the two lowest speeds are burdened with a greater measurement error than the others, because low differences between the obtained voltages of individual tests cause significant differences in the calculated forces acting on model, which ultimately leads to visible differences in the values of the drag coefficient. Figure 13 shows and average values from obtained results compared with experimental results presented in works: BELLO (2011), BELLO-MILLÁN (2016), MÄKELÄ (2013), MEILE (2011), THACKER et al. (2012).

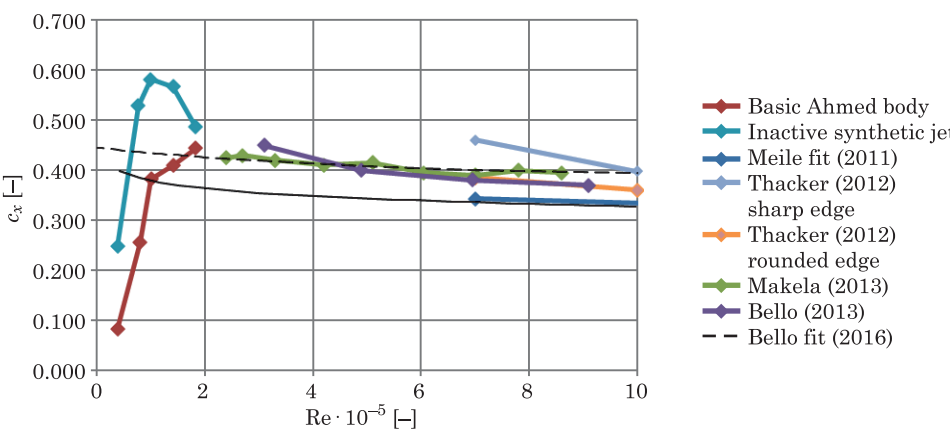

Fig. 13. Comparison of the averaged results with other author's results

Conclusions

For data taken from other author's, it can be seen that the value of the drag coefficient for the Ahmed body model decreases when the Reynolds number increases. The results obtained during the experiment show the opposite tendency. The proposed values of the Reynolds number are significantly lower than those typical for vehicle aerodynamics research and those presented in the literature. It should be noted, however, that in the course of the conducted experiment it was intentional to obtain the low Reynolds number in the range of $0.35\times10^5 - 1.8\times10^5$. It can also be noted that the obtained drag coefficient, for the largest values of Reynolds numbers are similar and starts to lean towards the range of values obtained by other author's. For the basic configuration of the model, the sudden drop in drag coefficient growth and the drop of c_x for the second configuration when the Reynolds number increases may suggest the occurrence of the drag crisis phenomenon, analogous to that occurring during the flow of a cylinder or a sphere. The lowest Reynolds numbers obtained in the conducted tests give values of the drag coefficient around 0.2. Such values of drag coefficients are characteristic for aerodynamic shapes, such as a streamlined body or airfoil, in which the laminar boundary layer does not detach. Importantly, for these cases, low drag forces are obtained, which could lead to erroneous results due to insufficient sensitivity of the force sensor. Mounting an synthetic jet outlet in the rear part of the model caused an increase in drag coefficient. This was due to a disturbance in the airflow on the model sloping wall where the boundary layer was detached too early, creating turbulent flow and ultimately increasing the aerodynamic footprint in comparison to the first configuration. A similar results can be seen in the work of VOZNYAK et al. (2021), examining the drag coefficient of the frontal resistance of the bus model with different ventilation schemes. The research shows that placing the air conditioning set in different locations of the bus roof always results in an increase of model resistance. The smallest increase of 0.9% was recorded in the front part. Placing ventilation equipment on the central section increased the drag coefficient by 3.7% and the assembly on the stern part resulted in the largest increase 5.7%. Considering the above results, the location of the synthetic jet outlet on the Ahmed body should be verified, as well as the outlet being designed in a way that does not adversely affect the drag coefficient of the model. The direction of further research should be a better implementation of active and fulfilling it's role synthetic jet which will ensure a stable air flow along the sloping wall of the model as in the works CUI et al. (2015), WANG et al. (2019).

References

AHMED S.R., RAMM G., FALTIN G. 1984. *Some salient features of the time-averaged ground vehicle wake*. SAE Transactions, 93: 473–503.

BELLO F. 2011. *Numerical study of Ahmed body*. Universidad de Malaga.

BELLO-MILLÁN F.J., MÄKELÄ T., PARRAS L., DEL PINO C., FERRERA C. 2016. *Experimental study on Ahmed's body drag coefficient for different yaw angles*. Journal of Wind Engineering and Industrial Aerodynamics, 157: 140-144. https://doi.org/10.1016/j.jweia.2016.08.005.

CUI W., ZHU H., XIA C., YANG Z. 2015. *Comparison of Steady Blowing and Synthetic Jets for Aerodynamic Drag Reduction of a Simplified Vehicle*. Procedia Engineering, 126: 388-392. https://doi.org/10.1016/j.proeng.2015.11.224.

KADIVAR M., TORMEY D., MCGRANAGHAN G. 2021. *A review on turbulent flow over rough surfaces: Fundamentals and theories*. International Journal of Thermofluids, 10: 100077. https://doi.org/10.1016/j.ijft.2021.100077.

MAHO H. 2016. *Concepts for generating lateral aerodynamic forces by means of an asymmetric airflow*. AIRSHAPER Department of Computational Fluid Dynamics.

MÄKELÄ T. 2013. *Experimental study of the flow around the Ahmed body*. Universidad de Malaga.

MEILE W., BRENN G., REPPENHAGEN A., LECHNER B., FUCHS A. 2011. *Experiments and numerical simulations on the aerodynamics of the Ahmed body*. CFD Letters, 3(1).

PIECHNA J. 2000. *Fundamentals of vehicle aerodynamics*. Wydawnictwo Komunikacji i Łączności. Warszawa.

SCHLICHTING H., GERSTEN K. 2000. *Boundary-Layer Theory*. 8th edition. Springer, Berlin, p. 29-50. https://doi.org/10.1007/978-3-642-85829-1.

SHADMANI S., MOUSAVI NAINIYAN S.M., GHASEMIASL R. 2018. *Experimental study of flow control over an Ahmed body using plasma actuator*. Mechanics and Mechanical Engineering, 22(1): 239-251.

SIVARAJ G., PARAMMASIVAM K.M., SUGANYA G. 2018. *Reduction of aerodynamic drag force for Reducing fuel consumption in road vehicle using basebleed*. Journal of Applied Fluid Mechanics, 11(6): 1489-1495. https://doi.org/10.29252/jafm.11.06.29115.

STURM H., DUMSTORFF G., BUSCHE P., WESTERMANN D., LANG W. 2012. *Boundary Layer Separation and Reattachment Detection on Airfoils by Thermal Flow Sensors*. Sensors, 12(11): 14292-14306. https://doi.org/10.3390/s121114292.

TALAY T.A. 1975. *Introduction to the aerodynamics of flight*. NASA History Division, Washington, D.C.

THACKER A., AUBRUN S., LEROY A., DEVINANT P. 2012. *Effects of suppressing the 3D separation on the rear slant on the flow structures around an Ahmed body*. Journal of Wind Engineering and Industrial Aerodynamics, 107-108: 237-243. https://doi.org/10.1016/j.jweia.2012.04.022.

VOZNYAK P., KAPALO P., DOVBUSH O., ADAMSKI M. 2021. *Frontal resistance coefficient of the buses with the different ventilation equipment*. Engineering Review, 41. https://doi.org/10.30765/er.1443.

WYSOCKI D. 2020. *Experimental studies to reduce the aerodynamic drag of a vehicle model using "synthetic jet"*. Mateusz Weiland Network Solutions. Poszerzamy Horyzonty, 21(3): 83-99.

WANG B., YANG Z., ZHU H. 2019. *Active flow control on the 25° Ahmed body using a new unsteady jet*. International Journal of Heat and Fluid Flow, 79: 108459. https://doi.org/10.1016/j.ijheatfluidflow.2019.108459.

ZHU L.D., LI L., XU Y.L., ZHU Q. 2012. *Wind tunnel investigations of aerodynamic coefficients of road vehicles on bridge deck*. Journal of Fluids and Structures, 30: 35-50. https://doi.org/10.1016/j.jfluidstructs.2011.09.002.